Draft version September 2, 2026
Typeset using LATEX **preprint** style in AASTeX631

Skyfire: A Spectroscopic Census of Little Red Dots and Broad-Line AGN in the CEERS Field

Dale D. Kocevski,[1] Anthony J. Taylor,[2,3] Masafusa Onoue,[4] Kohei Inayoshi,[5] Steven L. Finkelstein,[2,3] Guillermo Barro,[6] Jingsong Guo,[7] Pablo Arrabal Haro,[8,*] Jonathan R. Trump,[9] Rebecca L. Larson,[10,†] Mark Dickinson,[11] Casey Papovich,[12,13] Fabio Pacucci,[14,15] Pablo G. Pérez-González,[16] Michaela Hirschmann,[17] Elizabeth J. McGrath,[1] Brenda L. Jones,[18] Nikko J. Cleri,[19,20,21] Kelcey Davis,[9,22,‡] Mauro Giavalisco,[23] Norman A. Grogin,[24] Taylor A. Hutchison,[8,*] Jeyhan S. Kartaltepe,[25] Allison Kirkpatrick,[26] Gene C. K. Leung,[27] Rachel S. Somerville,[28] and Stephen M. Wilkins[29,30,31]

ABSTRACT

We present the Skyfire program, a 21-hour Cycle 3 JWST/NIRSpec survey with the G395M medium-resolution grating covering five pointings in the Extended Groth Strip. The survey is designed to carry out a systematic census of faint, broad-line AGN candidates with a range of rest-optical colors identified photometrically at $z > 3$ by the Cosmic Evolution Early Release Science (CEERS) Survey. Our primary targets include photometrically-selected Little Red Dots (LRDs), blue extreme emission line galaxies (EELGs), and X-ray-detected AGN. We present spectroscopic redshifts for 178 sources observed by Skyfire, as well as a catalog of 34 sources with broad emission lines in the redshift range $2.7 < z < 6.5$. Our broad-line sample includes 18 LRDs, which brings the spectroscopic completeness of LRDs with $\beta_{\rm opt} > -0.02$ in the CEERS field to 73%. We explore the prevalence of broad emission lines in photometrically-selected LRDs as a function of their rest-frame continuum slope and observed color distributions. We find the broad-line detection fraction in LRDs remains high at relatively blue rest-optical colors and extends smoothly into the bluer regime occupied by Little Blue Dots (LBDs). We discuss the implications of this finding for LRD-LBD unification scenarios. We also find that only 18% (3/17) of EELGs selected primarily for their high-equivalent-width emission lines and compact morphologies exhibit broad emission lines, suggesting these criteria alone are poor predictors of broad-line activity. We present a revised set of LRD selection criteria that captures bluer sources by extending down to $\beta_{\rm opt} = -0.52$. Using this new threshold, we find that $80.9^{+4.6}_{-7.5}$% of photometrically-selected LRDs brighter than 26.5 in F444W show broad emission lines and that LRDs make up 54% of the overall broad-line population identified in the CEERS field.

Keywords: High-redshift galaxies (734); Quasars (1319); Supermassive black holes (1663)

1. INTRODUCTION

It is now well established that supermassive black holes (SMBHs) reside at the centers of nearly all massive galaxies and that the growth of these black holes (BHs) is intimately connected to the evolution of their hosts (e.g., Hopkins et al. 2008; Di Matteo et al. 2008; Kormendy & Ho 2013; Madau & Dickinson 2014). As a result, SMBHs and the active galactic nuclei (AGN) that they power have become key components in most galaxy evolution models (e.g., Somerville et al. 2008; Dubois et al. 2016; Chen et al. 2020; Davé et al. 2019). However, several open issues remain in our understanding of their formation and early growth, including the nature of the BH seed population and how the BH-galaxy scaling relationships observed in the local universe (Kormendy & Richstone 1995; Magorrian et al. 1998; Gebhardt et al. 2000; Ferrarese & Merritt 2000) are established and maintained. Addressing these questions requires characterizing the growth of SMBHs from their earliest seeds through the peak of cosmic activity, and constraining the distribution of BH masses and their accretion rates in the first billion years of cosmic history (Volonteri 2010; Inayoshi et al. 2020; Habouzit et al. 2022).

jonathan.trump@uconn.edu

* NASA Postdoctoral Fellow
† Giacconi Postdoctoral Fellow
‡ NSF Graduate Research Fellow

Prior to the launch of the James Webb Space Telescope (JWST; Gardner et al. 2023), our understanding of BH growth in the early universe was largely shaped by wide-field quasar surveys carried out at optical and near-infrared wavelengths (Fan et al. 2001; Willott et al. 2010; Jiang et al. 2016; Matsuoka et al. 2016; Yang et al. 2023b). These surveys revealed hundreds of quasars at $z > 5$ powered by BHs with masses of order 10^9 $M_\odot$, but remain sensitive to only the most luminous and extreme systems. JWST has fundamentally changed this picture by enabling the detection of a large population of faint broad-line AGN at $z > 3$ (Kocevski et al. 2023; Übler et al. 2023; Harikane et al. 2023; Maiolino et al. 2024; Greene et al. 2024; Matthee et al. 2024; Taylor et al. 2025a; Hviding et al. 2025). These sources are orders of magnitude less luminous and more common than bright quasars and are powered by the least massive SMBHs known in the early universe (Onoue et al. 2023; Taylor et al. 2025a; Jones et al. 2025). Because they are more representative of the underlying BH population than luminous quasars, these faint AGN offer a promising route to constraining models of BH seeding (Pacucci & Loeb 2022; Li et al. 2024) and the early coevolution of SMBHs with their host galaxies (Habouzit et al. 2022; Inayoshi et al. 2022; Pacucci et al. 2023).

A substantial fraction of these broad-line AGN appear heavily reddened in the rest-frame optical with relatively blue colors in the rest-frame ultraviolet (Kocevski et al. 2023; Furtak et al. 2023; Greene et al. 2024; Matthee et al. 2024; Kocevski et al. 2025). Compact sources with this "v-shaped" spectral energy distribution have come to be known as little red dots (LRDs; Matthee et al. 2024) and represent one of the most unexpected discoveries of the JWST era. Photometric searches have found LRDs to be remarkably ubiquitous at high redshifts, reaching number densities of order 10^{-5} Mpc^{-3} at $z \sim 5-6$ (Barro et al. 2024; Kokorev et al. 2024; Labbe et al. 2025) before declining rapidly below $z \sim 4$ (Kocevski et al. 2025; Ma et al. 2025; Zhuang et al. 2025; Weibel et al. 2026; although see Bisigello et al. 2025).

Spectroscopic follow-up confirms that 70–90% of photometrically selected LRDs exhibit broad Balmer emission lines (Greene et al. 2024; Kocevski et al. 2025; Hviding et al. 2025). While the precise nature of LRDs remains a topic of intense debate (e.g., Naidu et al. 2025; Madau & Maiolino 2026; Pacucci et al. 2026; Pérez-González et al. 2026), the detection of extreme Balmer breaks in some LRDs with strengths that exceed those achievable with evolved stellar populations (Naidu et al. 2025; de Graaff et al. 2025a; Taylor et al. 2025b) suggests that they are likely powered by a previously unrecognized population of gas-enshrouded, accreting SMBHs (Inayoshi & Maiolino 2025; Kokorev et al. 2026; de Graaff et al. 2025b).

Recently, Barro et al. (2026) reported broad-line detections among LRDs with bluer rest-optical colors than the red colors cuts used by canonical LRD selection criteria (Labbe et al. 2023; Kocevski et al. 2025), indicating that LRDs constitute a more diverse population than initially recognized, extending beyond the most extreme red objects. The relationship between LRDs and their bluer, broad-line emitting counterparts, recently dubbed "little blue dots" (LBDs, Asada et al. 2026; Brazzini et al. 2026), remains unsettled. Recent studies have argued that LRDs and LBDs may not be physically distinct populations, with viewing angle and line-of-sight gas density plausibly responsible for turning an intrinsically blue, compact broad-line AGN into a red one (Billand et al. 2026; Madau & Maiolino 2026). A key difficulty in establishing a unification scenario is that while LRDs have generally been targeted for spectroscopic follow-up due to their distinctive colors, compact AGN candidates with bluer rest-frame optical continua more closely resemble ordinary star-forming galaxies and have typically only turned up serendipitously within larger spectroscopic campaigns (e.g., Taylor et al. 2025a; Hviding et al. 2025). This implies that an unknown fraction of the broad-line AGN population has been missed by red-color-based searches. Resolving this will require spectroscopic samples that span the full range of rest-frame optical colors among compact, high-redshift AGN candidates, rather than samples preselected for their red colors alone.

In this paper, we present the Skyfire program (GO-5718; PIs Kocevski & Guo), a Cycle 3 JWST/NIRSpec multi-object spectroscopic survey with the G395M medium-resolution ($R \sim 1000$) grating in the Extended Groth Strip (EGS) field. The survey is designed to carry out the first systematic census of faint broad-line AGN candidates with a range of rest-optical colors identified photometrically by the Cosmic Evolution Early Release Science (CEERS) Survey (Bagley et al. 2022; Finkelstein et al. 2025a). The motivation for the survey is to increase the spectroscopic completeness of LRDs, LBDs, and extreme emission line galaxies in the CEERS field in order to complete the census of faint, broad-line emitting AGN in the early Universe.

In Section 2, we present the Skyfire survey design and target selection, while Section 3 describes the NIRSpec observations and our data reduction. Section 4 discusses our methodology to measure spectroscopic

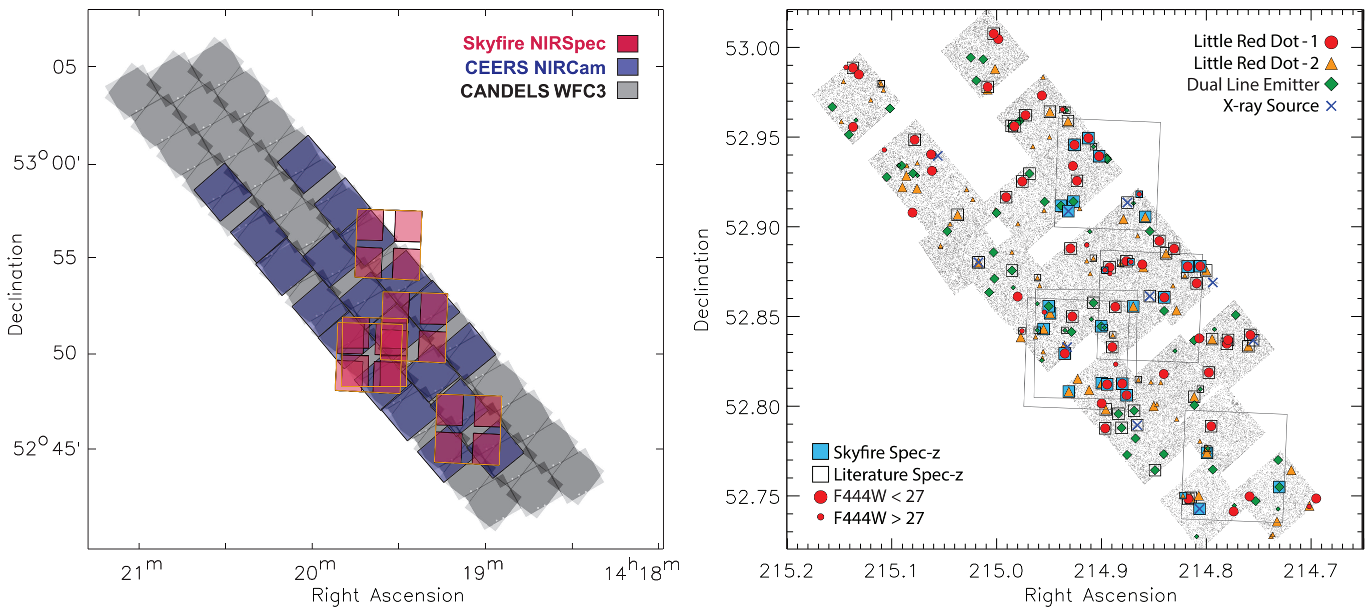

Figure 1. (*left*) The pointing centers of the five NIRSpec MSA masks observed by Skyfire relative to the JWST/NIRCam imaging from CEERS (blue) and HST/WFC3 imaging from CANDELS (grey). (*right*) The distribution of high priority targets in the CEERS field. LRD-1 sources are drawn from the LRD sample of Kocevski et al. (2025), while LRD-2 sources are drawn from the LRD samples of Kokorev et al. (2024) and Barro et al. (2024). Dual line emitters are blue, broad-line AGN candidates with strong emission lines from the catalog of Guo et al. (2025). Sources observed by Skyfire are shown with filled blue squares, while those with prior spectroscopic observations are highlighted with open squares. Larger/smaller symbols are used for sources brighter/fainter than 27th magnitude in F444W.

redshifts and broad-line widths. Section 5 presents our spectroscopic redshift catalog and broad emission line sample, while Section 6 presents a handful of individual sources of interest. Throughout this paper we use the following cosmological parameters: $H_0 = 70$ km s^{-1} Mpc^{-1}; $\Omega_{\rm tot}, \Omega_\Lambda, \Omega_{\rm m} = 1, 0.7, 0.3$.

2. SURVEY DESIGN

Skyfire is designed to perform a spectroscopic census of faint AGN through the detection of their broad emission lines. The survey utilizes NIRSpec observations with the G395M/F290LP grating/filter pair, which provides optimal spectral coverage ($3-5\mu$m) and resolution ($R \sim 1000$) needed for this purpose. The spectral coverage allows both the Hα line and the Hβ+[OIII] multiplet to be detected at $z \sim 5$ and the Hβ line out to $z \sim 9.4$, while the velocity resolution ($\Delta v \sim 300$ km s^{-1}) is sufficient to resolve broad emission (FWHM ~ 1000 km s^{-1}) originating near the AGN accretion disk from a narrow component from the host galaxy. It also allows for the deblending of the Hβ+[OIII] complex and the detection of broad components in the individual [OIII] lines. The lack of broad emission in these forbidden lines can help rule out galactic outflows as the source of any broad emission observed in the Balmer lines.

The EGS was chosen as the target field for Skyfire due to the wealth of multi-wavelength data available in the field. This includes 1-4 μm NIRCam imaging from CEERS (Bagley et al. 2022; Finkelstein et al. 2025b), 5–21μm MIRI observations from both CEERS (Yang et al. 2023a) and the MIRI EGS Galaxy and Active Galactic Nucleus (MEGA) survey (Backhaus et al. 2025), 0.6-1.6μm Hubble Space Telescope (HST) ACS and WFC3 imaging from the Cosmic Assembly Near-infrared Deep Extragalactic Legacy Survey (CANDELS; Grogin et al. 2011; Koekemoer et al. 2011), and deep (800 ksec) Chandra X-ray observations (Nandra et al. 2015). The field also has extensive optical and infrared spectroscopy from the All-Wavelength Extended Groth Strip International Survey (AEGIS; Davis et al. 2007), 3D-HST (Brammer et al. 2012), CEERS (Pirzkal et al. 2017; Arrabal Haro et al. 2023), the CANDELS-Area Prism Epoch of Reionization Survey (CAPERS; Donnan et al. 2025), the Red Unknowns: Bright Infrared Extragalactic Survey (RUBIES; de Graaff et al. 2025a), The High-(Redshift+Ionization) Line Search (THRILS; Hutchison et al. 2025), C3PO (Papovich et al., in prep), and the MEGA NIRSpec survey (Kirkpatrick et al., in prep).

2.1. *Target Selection*

The primary targets for Skyfire are LRDs and blue, broad-line AGN candidates. The LRD sample is split into two subsamples. The first subsample is the LRD

Table 1. Skyfire Observations

Visit	R.A. (J2000)	Dec. (J2000)	APA (deg)	Obs Date
1:1	14:19:34	52:55:35	267.67	2025-06-19
1:2	14:19:25	52:51:16	267.63	2025-06-21
1:3	14:19:41	52:49:42	267.69	2025-06-23
1:4	14:19:22	52:48:49	267.58	2025-06-24
1:5	14:19:39	52:49:59	89.20	2025-12-17

catalog from Kocevski et al. (2025), which we refer to hereafter as the LRD-1 sample. This sample consists of sources selected based on having a "v-shaped" spectral energy distribution (SED) with a strongly rising rest-optical continuum and a compact morphology. In a recent analysis by Hviding et al. (2025), it was reported that while this sample has a high accuracy in identifying LRDs with broad-line emission, it becomes increasingly incomplete towards bluer rest-optical colors. As a result, we supplement this sample with the LRD catalogs of Kokorev et al. (2024) and Barro et al. (2024), which use multi-color selection that picks up LRDs with bluer rest-optical colors. Hviding et al. (2025) find that while the completeness of this secondary subsample is higher than that of Kocevski et al. (2025), it suffers from a decreased accuracy, presumably due to contamination from galaxies with strong emission lines or dusty star-forming galaxies at lower redshifts. We refer to this subsample as the LRD-2 sample hereafter.

Our sample of blue, broad-line AGN candidates is drawn from the catalog of dual line emitters (DLE) from Guo et al. (2025). These sources are extreme emission line galaxies (EELGs) selected photometrically to have strong Hβ+[OIII] and Hα lines. The sample has a mean rest-frame equivalent width for Hβ and Hα of 990Å and 1050Å, respectively. The selection technique of Guo et al. (2025) was successfully used by Onoue et al. (2023) to discover a z=5.24 AGN, CEERS 2782, which was later confirmed to have broad emission lines by Kocevski et al. (2023). We refer to this subsample as the DLE sample hereafter. Finally, we added X-ray sources at $z > 2.5$ drawn from the AEGIS-X survey (Nandra et al. 2015) to our primary target sample.

We cross-matched our primary targets with a spectroscopic redshift compilation from the Dawn JWST Archive[1] (DJA; de Graaff et al. 2024; Heintz et al. 2024). Sources previously observed with NIRSpec's M or H gratings that resulted in spectra where the width of the Balmer lines could be measured were moved from our primary sample to our filler sample (described below). Sources observed with the lower-resolution NIRSpec PRISM were kept in the primary sample and their redshifts updated if the source previously lacked a spectroscopic redshift.

For our filler catalog, we employed a multiwavelength catalog described in detail in Hutchison et al. (2025). In short, a combined source catalog was constructed using public CEERS NIRCam and MIRI imaging and the CANDELS EGS catalogs of Stefanon et al. (2017) and Finkelstein et al. (2022). For the CEERS data, photometry and photometric redshifts were drawn from the UNICORN photometric catalog (see §3.1; S. Finkelstein et al., in prep.). For each source, near-infrared magnitudes were drawn preferentially from JWST/NIRCam where available or from HST/WFC3 or Spitzer/IRAC otherwise. Photometric redshifts were drawn from three catalogs in priority order — the CEERS UNICORN NIRCam-based redshifts, then the CANDELS HST+Spitzer values, then the CANDELS EGS catalog of Finkelstein et al. (2022). Spectroscopic redshifts followed the same tiered priority scheme, drawing first from the CEERS NIRSpec catalog, then the DJA, then CANDELS, and finally ground-based DEIMOS (Newman et al. 2013) and Keck/MOSFIRE (Sanders et al. 2021; Larson et al. 2022; Jung et al. 2018; Urbano Stawinski et al. 2024) programs.

MSA optimization was done in two stages. First we ran the eMPT software suite (Bonaventura et al. 2023) on our primary target list to identify pointing centers that would maximize the number of high-priority candidate AGN on slits given our assigned aperture position angle (APA). Primary targets with F444W < 27 were given uniform weighting as priority class 1 objects in eMPT, while fainter sources were assigned priority class 2. With candidate pointing centers computed, we then used the MSA Planning Tool (MPT) in APT to optimize the masks. We used a weighting scheme that downweights sources at lower redshift, as well as fainter sources that might not be detected. The formula used can be expressed as:

$$W = \sqrt{F_{\rm nJy} * z^6}. \quad (1)$$

where W is the MSA weight, $F_{\rm nJy}$ is the flux density in nanojanskies of the source in the F444W filter or Spitzer Ch2 when outside of the JWST coverage, and z is the best available redshift for each source. The weights were normalized to range from 1 to 1000. Sources in our primary target sample were manually boosted by an additional factor of 1000. Optimal masks were defined as those that achieved the highest combined weight for all

[1] https://dawn-cph.github.io/dja

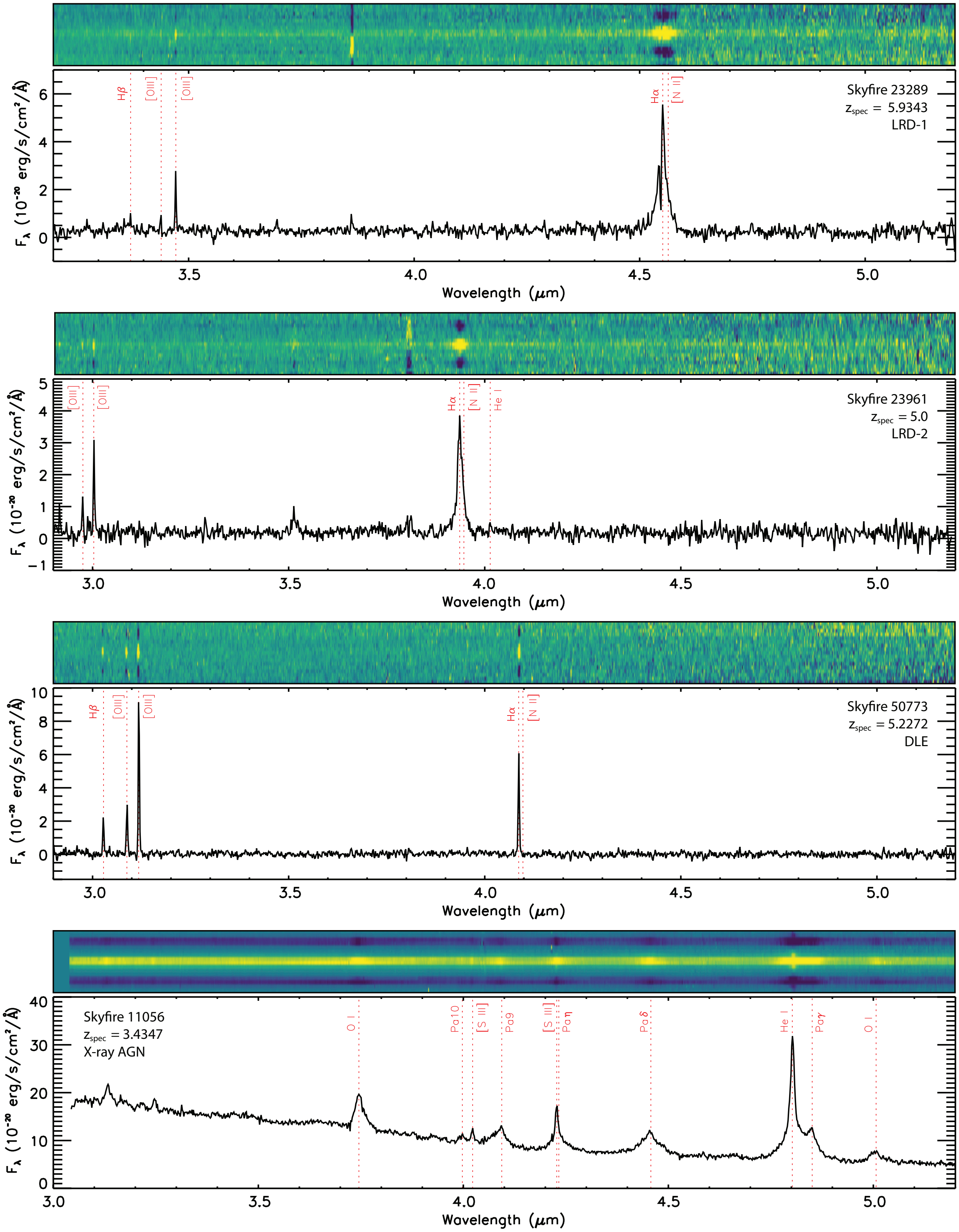

Figure 2. Example Skyfire NIRSpec spectra taken in the G395M grating. The sources shown are examples of each of the four high-priority target classes observed by Skyfire: LRD-1, LRD-2, DLEs, and X-ray AGN. The locations of several prominent emission lines are noted.

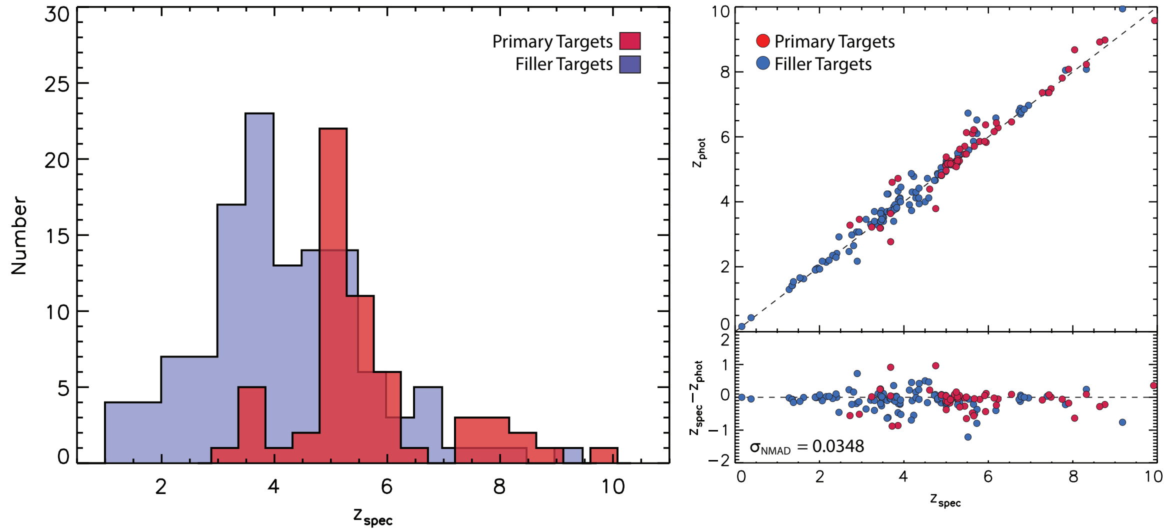

Figure 3. (*left*) The spectroscopic redshift distribution of the primary (red) and filler (blue) sources observed by Skyfire. (*right*) A comparison of the photometric and spectroscopic redshifts of the sources observed by Skyfire. We find good agreement between our measured spectroscopic redshifts and our prior photometric redshifts, measuring a normalized median absolute deviation of $\sigma_{\rm NMAD} = 0.0348$.

targets allocated MSA shutters. Through this process, we identified six pointing centers that maximized the number of high-priority candidate AGN on slits and the combined weights of our filler targets.

3. OBSERVATIONS & DATA REDUCTION

The initial round of Skyfire observations were carried out on 2025 June 19-24. We used 3-shutter slitlets and a 3-shutter nodding pattern for each pointing with the NRSIRS2 readout pattern. We used 16 groups per integration and 2 integrations per exposure, resulting in a total exposure time of 7090 sec. Six pointings were attempted at an APA of 267°, but two suffered MSA target acquisition failures. One of these pointings was re-executed on 2025 Dec 17 at an APA of 89°. The pointing centers of our final five MSA masks are shown in Figure 1 and listed in Table 1. The number of our primary targets observed in each mask ranges from 11 to 15, while the total number of targets observed ranges from 54 to 61. The location of the primary targets observed in each pointing is shown on the right side of Figure 1.

The Skyfire data was reduced as described in Taylor et al. (2025a) using version 1.20.2 of the JWST Science Calibration Pipeline with the Calibration Reference Data System (CRDS) mapping 1464, starting from the Level 1 uncalibrated data products ("_uncal.fits" files) available on MAST.

The reduced two-dimensional (2D) spectra ("s2d") have a rectified trace with straight spatial and wavelength axes. To optimize the extraction of one-dimensional (1D) spectra from the 2D spectra, we perform a weighted extraction based on the methodology of Horne (1986). Briefly, for a given spectrum, we take the median of the 2D spectrum along the spectral direction to produce a spatial profile for the source. We then identify the central peak of this profile, which corresponds to the source's spectral trace. We then set all pixels in the spatial profile that are not a part of this central feature to zero and normalize the area under this masked spatial profile to one. We then use the normalized profile as the variable **P** in Table 1 of Horne (1986) and follow the prescription given therein to extract an optimized 1D spectrum. Examples of our reduced 1D and 2D spectra, for each high-priority target category (LRD-1, LRD-2, DLEs, and X-ray AGN), are shown in Figure 2.

3.1. *NIRCam Imaging & Photometric Redshifts*

In this study, we make use of *JWST* NIRCam imaging from the Cosmic Evolution Early Release Science Survey (CEERS; Finkelstein et al. (2025b)). The NIRCam data were processed using the *JWST* Calibration Pipeline[2] (versions 1.8.5 and 1.10.2, respectively) with custom modifications described in Finkelstein et al. (2025b) and Bagley et al. (2022). The resulting images were registered to the same World Coordinate System reference frame (based on Gaia DR1.2; Gaia Collaboration et al. 2016) and combined into a single mosaic for each field using the drizzle algorithm with an inverse variance map weighting (Fruchter & Hook 2002; Casertano et al.

[2] http://jwst-pipeline.readthedocs.io/en/latest/

Table 2. The Skyfire Survey Spectroscopic Redshift Catalog

ID	RA (J2000)	Dec (J2000)	$z_{\rm spec}$	$z_{\rm qual}$	$z_{\rm phot}$	F444W	Source Flag
299	214.805753	52.878045	5.6229	4	6.10	26.12	1
467	214.903179	52.946261	5.1027	4	5.17	26.18	3
1090	214.912510	52.949436	6.2290	4	6.28	26.80	1
1867	214.817678	52.877856	5.4457	4	5.47	25.55	1
2086	214.858256	52.905539	5.4806	4	6.13	24.31	2
2847	214.875185	52.913482	2.9434	4	3.46	23.57	4
3023	214.853818	52.897569	5.2931	4	5.26	26.76	3
3519	214.925759	52.945659	5.0885	4	5.26	26.01	1
4979	214.879011	52.904279	5.6548	4	6.22	26.92	2
5632	214.932394	52.938252	4.8883	4	4.82	24.49	5

Note—Source Flag: 1 = LRD-1, 2 = LRD-2, 3 = DLE, 4 = X-ray AGN, 5 = Filler. This table is available in its entirety at https://github.com/dalekocevski/Kocevski26

2000) via the Resample step in the pipeline. The final mosaics in all fields have pixel scales of 0.″03/pixel.

Source detection and photometry on the NIRCam mosaics were computed on PSF-matched images using `SExtractor` (Bertin & Arnouts 1996) version 2.25.0 in two-image mode, with an inverse-variance weighted combination of the PSF-matched F277W and F356W images as the detection image. Photometry was measured in all of the available NIRCam bands in each field, as well as the F606W and F814W HST bands using public data from the CANDELS surveys (Grogin et al. 2011; Koekemoer et al. 2011). Two runs of `SExtractor` were conducted in a hot+cold setup similar to the process described in Galametz et al. (2013). Sources are first selected with conservative (cold) detection parameters, designed not to split up large, bright galaxies, followed by a more aggressive (hot) run, which is performed to identify fainter objects. Objects from the hot catalog that fall outside the segmentation map from the cold run are added to the final photometry catalog. Our analysis of the NIRCam imaging data is similar to that described in Finkelstein et al. (2024); hence, we refer the reader there for additional details.

Photometric redshifts were computed using the EAZY (Brammer et al. 2008) software package for all sources in our photometric catalogs. EAZY fits non-negative linear combinations of user-supplied templates to derive probability distribution functions (PDFs) for the redshift, based on the quality of fit of the various template combinations to the observed photometry for a given source. We use the default template set "tweak_fsps_QSF_12_v3", which consists of 12 templates derived from the stellar population synthesis code FSPS (Conroy et al. 2010), as well as the six bluer templates created by Larson et al. (2022), as described in Finkelstein et al. (2023). A flat redshift prior with respect to luminosity was assumed and redshifts from $z = 0$ to 20 were considered. We also perform a "low-redshift" run with the maximum redshift set to $z = 7$ to allow for visualization of the best-fitting low-redshift model for sources found to be at $z > 9$.

4. REDSHIFT AND LINE MEASUREMENTS

An initial measurement of spectroscopic redshifts was carried out using an automated emission line fitting algorithm. The software uses the cataloged photometric redshift of each source to identify emission lines and fit their centroids. The spectra of all sources were then manually inspected to check the automated redshift calculation, measure redshifts for sources where the algorithm failed to compute a redshift, and grade the quality of the redshift measurement. We assigned quality flags based on the strength (i.e., signal-to-noise ratio, S/N) and number of the identified emission lines and the agreement with existing photometric redshift estimates. The quality scheme for the derived redshifts is as follows:

- 4.0: Multiple high S/N ($\gtrsim 3$) emission lines
- 3.0: Multiple low S/N ($\lesssim 3$) emission lines.
- 2.0: Single emission line + z_{spec} agrees with z_{phot}
- 1.0: Unidentified features
- 0.0: No features

Sources with quality ≤ 1 have their redshifts set to NaN in our final redshift catalog (see §5).

In addition to redshift measurements, we also perform a search for broad emission lines across the entire target sample (primary and filler). We measure line fluxes and widths in the G395M/F290LP spectra using a Levenberg-Marquardt least-squares method implemented by the `mpfit` IDL code[3] as described in Kocevski et al. (2023). We simultaneously fit multiple Gaussians for features in the Balmer and Paschen line regions, depending on the redshift of the source. To account for broad components, we fit lines with two Gaussians: one narrow with width < 350 km s^{-1} and one broad with width > 350 km s^{-1}. The line centers, widths, and fluxes are all free parameters and the broad and narrow components can be kinematically offset from each other. When fitting Hα we also include additional Gaussian components for the [N II] $\lambda\lambda$6550, 6585 doublet. While the Hα and [N II] λ6585 lines are separated by roughly three times the resolution limit, the lines will blend together in the presence of a sufficiently broad Hα component. We account for this by constraining the line widths and relative line centers of the [N II] doublet to that of narrow Hα. If a source shows signs of blue-shifted absorption in their Balmer lines similar to the ones reported in Matthee et al. (2023) and Kocevski et al. (2025), we add an additional absorption component to our model.

Uncertainties on our line measurements are derived using a Monte Carlo approach. For each spectral element, we perform 1000 random draws from a Gaussian distribution whose mean is set to the measured flux at that wavelength and whose standard deviation is set to the error in that measurement. Our line fitting is then repeated on all 1000 mock spectra, and standard deviations are calculated as half the 16th-to-84th percentile range of the resulting distributions.

To test the statistical significance of the broad line components, we used the approach described in Taylor et al. (2025a). We fit each source with a model that includes and excludes the broad component and compute the Bayesian Information Criterion (BIC) for each model fit. We next use the difference in the BIC between the models to determine which model fits best for each candidate line (with the lower BIC model preferred). We require a ΔBIC > 6 in favor of the broad-line model over the narrow line model and a $S/N > 5$ for the broad component, suggesting that the inclusion of the broad-line significantly improves the overall spectral fit without overfitting or adding unnecessary components to the model.

5. REDSHIFT CATALOG

In this section, we provide the redshift catalog for the Skyfire target sample. Skyfire observed 292 unique sources over 5 masks. Of these, 41 are LRDs (24 from the LRD-1 sample and 17 from the LRD-2 sample), 26 are DLEs, and 4 are X-ray AGN. We successfully measured spectroscopic redshifts (quality > 1) for 178 sources. Another 30 sources have unidentified features (quality $= 1$) and 84 sources lacked features from which to base a redshift measurement (quality $= 0$). The redshift distribution of our primary and filler samples is shown in Figure 3.

Our spectroscopic redshifts allow us to assess the accuracy of the photometric redshifts of our target sample. A comparison between the photometric and spectroscopic redshifts is shown on the right panel of Figure 3. We can quantify the agreement between the two using the normalized median absolute deviation ($\sigma_{\rm NMAD}$; Ilbert et al. 2009), defined as $1.48 \times {\rm median}(|\Delta z|/(1 + z_{\rm spec}))$. We find that our measured redshifts are in overall good agreement with our photometric redshift estimates, with $\sigma_{\rm NMAD} = 0.0348$, which is typical of robust photometric redshifts based solely on broadband photometry (e.g., Dahlen et al. 2013). We note that $\sigma_{\rm NMAD}$ for the primary sample is lower than that for the filler sample: 0.0165 versus 0.0397, respectively. This is largely driven by the DLE sample, which has a $\sigma_{\rm NMAD}$ of 0.0138. These sources are selected photometrically due to boosted line emission affecting the F277W and F410M filters, which preferentially identifies sources in a narrow redshift range near $z \sim 5$, resulting in a relatively low scatter. The LRD sample (LRD-1 plus LRD-2) has a scatter comparable to the filler sample, with $\sigma_{\rm NMAD}$ of 0.0281. This suggests that the usual SEDs of LRDs do not result in an increased photometric redshift uncertainty as is commonly found with other forms of AGN (e.g., Salvato et al. 2009).

We present our spectroscopic redshift catalog in Table 2. The details of the table columns are given below:

1. Skyfire ID
2. Right ascension (J2000)
3. Declination (J2000)
4. Spectroscopic Redshift
5. Spectroscopic Redshift quality flag (see §4)
6. Photometric Redshift
7. Magnitude (AB; F444W or Spitzer Ch2)
8. Source Category Flag (see below)

For the source category flag, we assign the following flags to each type of source observed: flag 1 are LRD-1, flag 2 are LRD-2, flag 3 are DLEs, flag 4 are X-ray sources, and flag 10 are filler targets.

6. BROAD-LINE AGN SAMPLE

One of the primary science goals of Skyfire is the detection and characterization of faint, broad-line AGN.

[3] https://pages.physics.wisc.edu/~craigm/idl/fitting.html

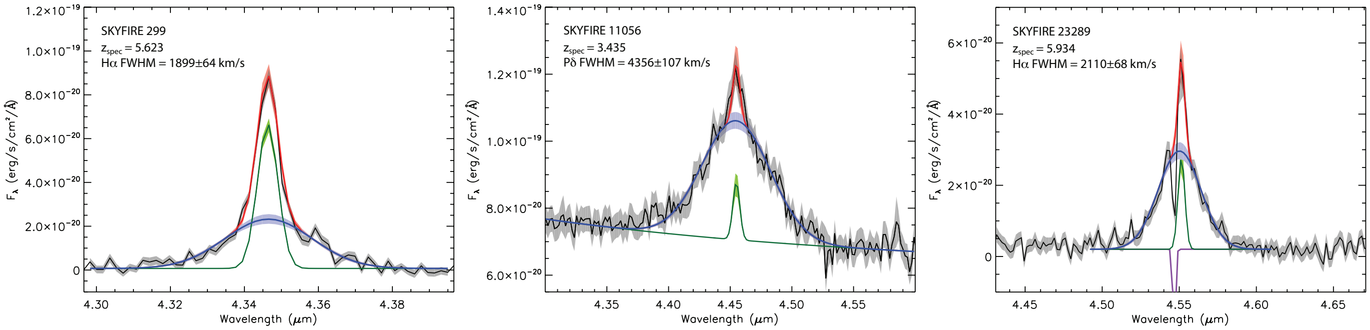

Figure 4. Example NIRSpec spectra with uncertainties (grey shaded region) taken in the G395M grating of three sources that feature broad emission lines. Green lines show the best-fit Gaussian for the narrow emission line component, blue lines show the best-fit broad component, and red lines show the best overall (narrow plus broad) fit to the emission line. The FWHM of the broad component (corrected for instrument broadening) is shown in the upper left of each panel.

In this section, we present a sample of broad-line emitters identified with Skyfire using the selection criteria outlined in §4. We find a total of 34 sources with broad emission lines in the redshift range $2.7 < z < 6.5$. Of these, 33 are new detections, while one source, Skyfire-549755, is a reobservation of RUBIES-EGS-28812 reported in Kocevski et al. (2025). Example G395M spectra of three sources with broad-line emission, in regions near their broad components, is shown in Figure 4, while the spectra of all 33 sources are shown in Figure 9 in Appendix A. Information about our broad-line sample, including our best-fit line widths and fluxes are listed in Table 3

The vast majority of the broad lines detected are Hα (29), while the others include the He Iλ10830 (3) and Paγ (2) lines. The broad-line widths that we measure for these lines range from 500 to 4000 km s^{-1}. Two sources in our sample, Skyfire-23082 and Skyfire-23289, also show absorption in their Balmer lines, a feature that has become increasingly common among LRDs (Matthee et al. 2023; Kocevski et al. 2025; Davis et al. 2026; Matthee et al. 2026).

Among the broad-line sources, 18 are LRDs (11 from LRD-1 and 7 from LRD-2), 3 are DLEs, 3 are X-ray sources, and 10 are filler targets. Of the 7 LRD-2 sources, we find that 4 would satisfy the LRD selection criteria of Kocevski et al. (2025) if a lower rest-optical slope cut is adopted ($\beta_{\rm opt} = -0.52$ instead of -0.02, which translates to F444W-F277W colors of 0.75 and 1.0, respectively). The remaining three sources were flagged by Kocevski et al. (2025) as potential extreme emission line galaxy (EELG) contaminants and therefore not included in their sample.

Of the 19 DLEs targeted for spectroscopic follow-up, redshifts were successfully measured for 17, of which only 3 exhibit broad emission lines. These sources are compact EELGs drawn from the sample of Guo et al. (2025) and have a mean Hα rest-frame equivalent width of 1050Å. This suggests that selecting sources based primarily on the presence of high-equivalent-width emission lines and compact morphologies is not particularly effective at isolating broad-line AGN and that samples selected in this manner are at risk of being contaminated by star-forming galaxies. That said, we note that 11 of our 19 DLE targets are relatively faint, with F444W < 27, resulting in low signal-to-noise spectra that may have limited our ability to detect broad components even if they were present. A firmer assessment of this method's robustness will require deeper spectroscopy of the fainter subsample to rule out sensitivity-driven incompleteness as the cause of the low broad-line detection rate. This result reiterates the difficulty of identifying blue broad-line AGN given that their colors make them hard to distinguish from the general galaxy population.

7. BLACK HOLE MASS ESTIMATES

We estimate the BH masses of our broad-line sample assuming that their broad emission lines trace the kinematics of gas that is gravitationally bound to and in virial orbits around the central BH. We follow the methodology of Jones et al. (2025) and make use of the single-epoch scaling relationship presented in Reines et al. (2013):

$$M_{\rm BH} = 3.7\times10^6 \left(\frac{L_{\rm H\alpha}}{10^{42}\ {\rm erg\ s^{-1}}}\right)^{0.47} \left(\frac{\rm FWHM_{H\alpha}}{10^3\ {\rm km\ s^{-1}}}\right)^{2.06} M_\odot. \quad (2)$$

Here $L_{\rm H\alpha}$ and FWHM$_{\rm H\alpha}$ are the luminosity and FWHM of the broad Hα line. Our measured BH masses for all sources where broad Hα is detected are listed in Table 3. Formal errors on our mass estimates are derived using the MCMC approach described in §4, but the Reines et al. (2013) relationship has an uncertainty of roughly 0.5 dex (Reines & Volonteri 2015) which will dominate over our measurement uncertainties.

Table 3. Catalog of Skyfire Sources with Broad Emission Lines

ID	R.A. (J2000)	Dec (J2000)	$z_{\rm spec}$	FWHM (km s^{-1})	$F_{\rm broad}$ (10^{-18} erg s^{-1} cm^{-2})	$\log(M_{\rm BH}/{\rm M}_\odot)$	Line
299	214.805753	52.878045	5.6229	1896 ± 63	6.63 ± 0.15	$7.31^{+0.03}_{-0.03}$	Hα
1090	214.912510	52.949436	6.2290	1141 ± 94	2.83 ± 0.16	$6.73^{+0.08}_{-0.09}$	Hα
1867	214.817678	52.877856	5.4457	1640 ± 185	2.23 ± 0.14	$6.94^{+0.11}_{-0.12}$	Hα
2086	214.858256	52.905539	5.4806	2111 ± 97	7.70 ± 0.28	$7.42^{+0.05}_{-0.05}$	Hα
2847	214.875185	52.913482	2.9434	1247 ± 157	2.93 ± 0.21	-	He I λ10830
3519	214.925759	52.945659	5.0885	1946 ± 126	3.84 ± 0.15	$7.17^{+0.06}_{-0.07}$	Hα
7761	214.840034	52.860648	3.8597	1985 ± 50	13.41 ± 0.20	$7.31^{+0.03}_{-0.03}$	Hα
9382	214.926772	52.914039	5.0730	596 ± 79	1.30 ± 0.22	$5.89^{+0.14}_{-0.17}$	Hα
11056	214.931614	52.908693	3.4347	4356 ± 107	24.66 ± 0.42	-	Paδ
12630	214.869654	52.855608	5.1033	2215 ± 443	1.35 ± 0.17	$7.08^{+0.19}_{-0.23}$	Hα
17484	214.799323	52.774004	5.0334	1524 ± 186	1.67 ± 0.10	$6.78^{+0.11}_{-0.13}$	Hα
20952	214.880185	52.812566	5.2802	1882 ± 123	4.42 ± 0.20	$7.19^{+0.07}_{-0.07}$	Hα
21749	214.876034	52.806109	5.7958	1601 ± 70	8.20 ± 0.19	$7.22^{+0.04}_{-0.04}$	Hα
22814	214.943538	52.849030	5.2413	1299 ± 269	2.70 ± 0.42	$6.75^{+0.20}_{-0.24}$	Hα
23082	214.949011	52.851744	3.7210	3948 ± 168	21.90 ± 1.24	$8.01^{+0.05}_{-0.05}$	Hα
23289	214.894556	52.812162	5.9343	2109 ± 68	9.69 ± 0.18	$7.51^{+0.03}_{-0.03}$	Hα
23961	214.899699	52.812840	5.0000	1702 ± 92	5.14 ± 0.18	$7.11^{+0.05}_{-0.06}$	Hα
24689	214.806408	52.742786	3.6858	1766 ± 74	6.74 ± 0.36	$7.05^{+0.05}_{-0.05}$	Hα
25941	214.934979	52.829364	5.9469	1424 ± 329	1.73 ± 0.14	$6.81^{+0.20}_{-0.25}$	Hα
26079	214.955188	52.843018	5.0015	2182 ± 84	12.45 ± 0.32	$7.51^{+0.04}_{-0.04}$	Hα
30148	214.931119	52.808158	6.5491	1671 ± 119	2.96 ± 0.17	$7.10^{+0.07}_{-0.08}$	Hα
44039	214.822229	52.750196	5.9128	1641 ± 271	1.76 ± 0.13	$6.93^{+0.15}_{-0.18}$	Hα
83652	214.871873	52.880432	5.6669	1202 ± 128	1.50 ± 0.11	$6.60^{+0.10}_{-0.12}$	Hα
92141	214.896761	52.875796	6.1365	1897 ± 217	1.13 ± 0.15	$6.99^{+0.12}_{-0.14}$	Hα
504101	214.947772	52.836333	4.8814	2437 ± 192	2.49 ± 0.15	$7.27^{+0.08}_{-0.09}$	Hα
504403	214.809743	52.739684	2.7007	1103 ± 199	1.48 ± 0.18	-	He I λ10830
513817	214.884590	52.844341	3.6240	1441 ± 119	2.45 ± 0.32	$6.65^{+0.10}_{-0.11}$	Hα
514153	214.746291	52.747477	3.2128	2601 ± 273	3.24 ± 0.24	-	Paδ
530722	214.871720	52.914307	4.3569	574 ± 67	3.09 ± 1.09	$5.96^{+0.16}_{-0.20}$	Hα
534080	214.949994	52.855774	5.2761	1388 ± 271	0.72 ± 0.15	$6.55^{+0.20}_{-0.24}$	Hα
542588	214.857161	52.903543	3.6015	979 ± 165	2.68 ± 0.68	$6.32^{+0.19}_{-0.22}$	Hα
547783	214.755946	52.759043	3.6886	1676 ± 153	1.20 ± 0.12	$6.65^{+0.10}_{-0.11}$	Hα
549030	214.883004	52.830524	3.7898	400 ± 50	1.17 ± 0.20	$5.37^{+0.14}_{-0.16}$	Hα

We note several important caveats regarding our reported BH masses. First, in calculating our BH masses, we do not correct our line luminosities for dust attenuation. The level of dust obscuration in LRDs remains uncertain and there is a growing consensus that their red colors are the result of being embedded in a dense gas cocoon as opposed to dust extinction (Inayoshi & Maiolino 2025; Naidu et al. 2025; de Graaff et al. 2025a; Taylor et al. 2025b; Kokorev et al. 2026). Given that LRDs comprise a significant portion of our sample, we have opted not to correct our measured line luminosities for dust attenuation.

Second, the broad emission lines of many LRDs show signatures of exponential wings that may arise due to scattering effects as opposed to virial motions (Rusakov et al. 2025; Kokorev et al. 2026). We have decided not to explore the prevalence of exponential profiles in the Skyfire spectra, instead saving that analysis for a future paper. As a result, our BH masses can be treated as upper limits if there is significant electron scattering or other nonvirial contribution to the line widths.

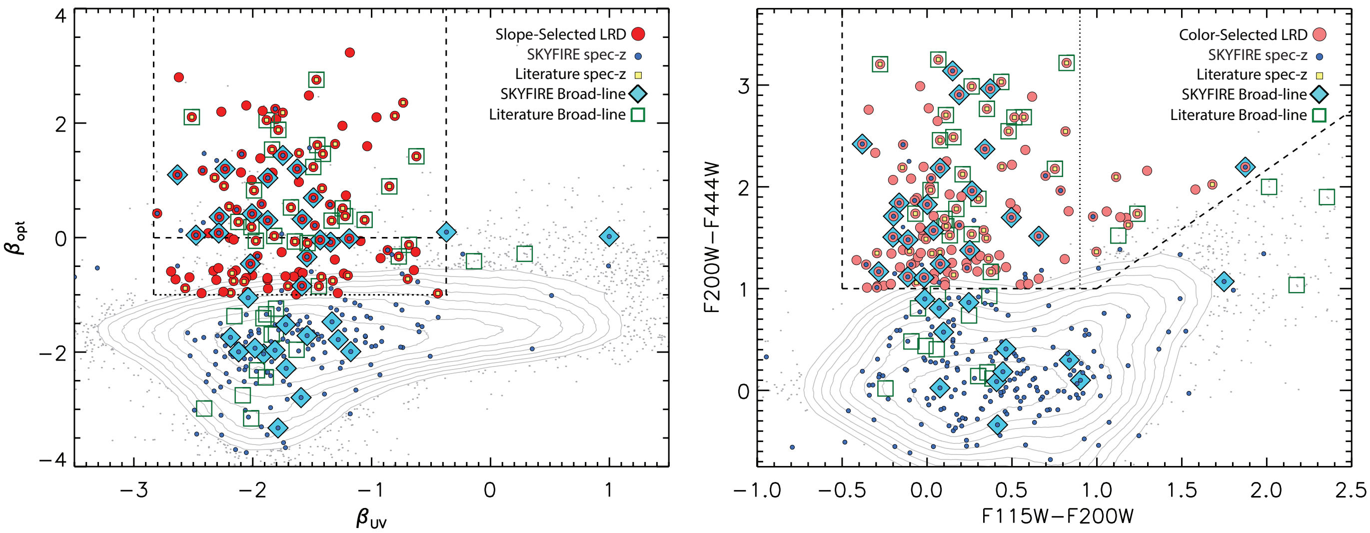

Figure 5. (*left*) The rest-frame optical and UV spectral slopes, $\beta_{\rm opt}$ and $\beta_{\rm UV}$ measured in the CEERS field for galaxies at $z > 2$ detected in the F444W filter with a SNR > 12. The horizontal and vertical dashed lines denote the LRD selection criteria of Kocevski et al. (2025), while the dotted line is a lower rest-optical threshold of $\beta_{\rm opt} = -0.52$. The red circles are sources that satisfy the slope-based LRD selection criteria of Kocevski et al. (2025) with this lower $\beta_{\rm opt}$ cut. Sources with spectroscopic redshifts from Skyfire and the literature are shown as small blue circles and yellow squares, respectively. Sources with broad emission lines from Skyfire and the literature are highlighted with filled blue diamonds and unfilled green squares, respectively. (*right*) The F115W-F200W versus F200W-F444W color distribution of the same galaxies shown in the left panel. The light red circles are sources that satisfy the color-based LRD selection criteria of Barro et al. (2026). The dashed lines denote that study's selection wedge. We find that the broad-line detection fraction remains high below the canonical cuts used to identify LRDs and likely extends smoothly into the bluer regime occupied by LBDs, suggesting these sources may be a continuous distribution of broad-line emitters and not be two distinct classes of objects

Third, the single-epoch virial mass relationship of Reines et al. (2013) was calibrated on relatively local AGN ($z < 0.06$) and may no longer be applicable at high redshifts. That said, Juodžbalis et al. (2025) recently reported a direct BH mass measurement for an LRD at $z = 7.01$ and found it to be in excellent agreement with the mass inferred from single-epoch virial estimates. This suggests that these relationships may in fact be reliable for LRDs out to relatively high redshifts.

8. CONTINUUM SLOPE & COLOR DISTRIBUTION OF BROAD-LINE LRDS

With the completion of Skyfire, 73% of the LRDs from the Kocevski et al. (2025) sample in the CEERS field have been observed spectroscopically with NIRSpec. In this section, we make use of this relatively high spectroscopic completeness to examine the prevalence of broad emission lines in photometrically-selected LRDs as a function of their observed colors and rest-frame continuum slopes.

To determine the continuum slope, β (where β is defined such that $f_\lambda \propto \lambda^\beta$), for a source, we perform a χ^2 minimization fit to the observed magnitudes using the linear relationship:

$$m_i = -2.5\ (\beta + 2)\ \log(\lambda_i) + c \qquad (3)$$

where m_i is the AB magnitude measured in the ith filter with an effective wavelength of λ_i. We perform this fit to determine both the rest-frame UV and optical spectral slopes, $\beta_{\rm UV}$ and $\beta_{\rm opt}$, using fluxes measured in bands blueward and redward of 3645Å based on the redshift of each source as described in Kocevski et al. (2025). Three bands are used to measure the slope in all cases except for sources at $z > 8$, where only the F356W and F444W bands are used to determine the rest-frame optical slope.

In the left panel of Figure 5, we show the rest-optical versus rest-UV continuum slopes of the broad line emitters identified with Skyfire. The red circles indicate LRDs identified in the CEERS imaging using the slope-based selection criteria of Kocevski et al. (2025) with their original optical slope cut of $\beta_{\rm opt} > -0.02$ (dotted line) and a lower threshold of $\beta_{\rm opt} > -1$ (dashed line). LRDs with spectroscopic redshifts are noted as indicated by the legend. Sources with broad emission lines at $z \gtrsim 3$ in the EGS field taken from the literature are also highlighted. These sources are drawn from Taylor et al. (2025a), Jones et al. (2025), Davis et al. (2026), and the recently completed MEGA NIRSpec survey (A. Kirkpatrick, private communication). The right panel of Figure 5 shows the F115W-F200W vs F200-F444W color distribution of the Skyfire broad line emitters, along

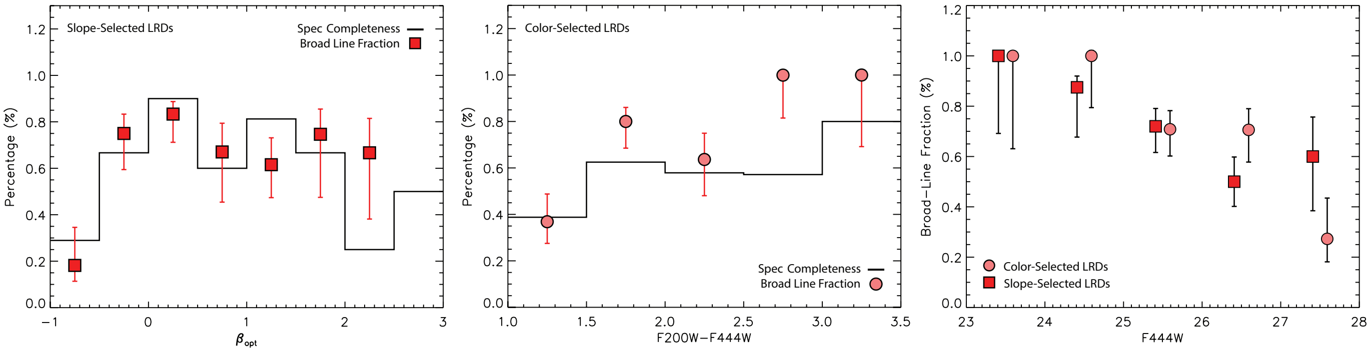

Figure 6. (*left*) The spectroscopic completeness and broad-line detection fraction of photometrically-selected LRDs identified using the continuum slope-based criteria of Kocevski et al. (2025) versus their rest-optical continuum slope, $\beta_{\rm opt}$. We find the broad-line fraction remains high below the original optical slope cut of $\beta_{\rm opt} > -0.02$ used in Kocevski et al. (2025) and only decreases in the $-1 < \beta_{\rm opt} < -0.5$ bin. (*middle*) The spectroscopic completeness and broad-line fraction of LRDs selected using the color criteria of Barro et al. (2026). We find a decreasing broad-line detection fraction at the bluest F200W-F444W colors.(*right*) The broad-line detection fraction among slope-selected (red) and color-selected (light red) LRDs as a function of their F444W magnitude.

with LRDs identified using the color-based selection criteria of Barro et al. (2026). The dashed lines in that panel denote the LRD selection wedge of Barro et al. (2026).

We can draw several conclusions from the observed slope and color distribution of the LRDs. First, the broad-line fraction among LRDs remains high below the original optical slope cut of Kocevski et al. (2025). This can be seen in the left-most panel of Figure 6, which shows the spectroscopic completeness and broad-line fraction of slope-selected LRDs versus $\beta_{\rm opt}$. Of the 18 LRDs with $-0.5 < \beta_{\rm opt} < -0.02$, 12 have been observed spectroscopically with the NIRSpec G395M grating and 9 show signs of broad-line emission ($75.0^{+8.3}_{-15.6}$% at 66.7% spectroscopic completeness). This is comparable to the broad-line detection fraction in redder LRDs: $73.3^{+5.5}_{-7.5}$% for LRDs with $-0.02 < \beta_{\rm opt} < 2.0$ at 78.8% spectroscopic completeness.

However, at the bluest slopes examined, $-1 < \beta_{\rm opt} < -0.52$, we find that the broad-line fraction drops precipitously to $18.8^{+16.4}_{-6.5}$%, albeit at a relatively low spectroscopic completeness of 28.9%. Of the 38 candidate LRDs with $-1 < \beta_{\rm opt} < -0.52$, 11 have G395M observations and only 2 show broad lines in their spectra. We conclude that the LRD candidates in this region are likely contaminated by normal galaxies with strong emission lines entering the LRD selection region, resulting in a decreased purity in terms of broad-line recovery.

We find a similar trend of decreasing broad-line detection fraction at the bluest F200W-F444W colors of photometrically-selected LRDs. This can be seen in the middle panel of Figure 6, which shows the spectroscopic completeness and broad-line fraction of color-selected LRDs versus their F200W-F444W color. At $\rm F200W - F444W > 1.5$, $81.4^{+4.5}_{-7.3}$% (at 61.4% spectroscopic completeness) of the color-selected LRD candidates have broad emission lines. However, at the bluest colors examined, $1.0 < \rm F200W - F444W < 1.5$, this fraction drops to $36.8^{+11.8}_{-9.3}$% at 38.8% spectroscopic completeness.

In addition, we find a low broad-line fraction among LRDs with both red F115W-F200W and F200W-F444W colors, which corresponds to the upper-right spur in the Barro et al. (2026) selection wedge. Of the 7 LRDs near this region that have been observed spectroscopically, two exhibit broad emission lines ($28.6^{+20.4}_{-10.7}$% at 58.3% spectroscopic completeness). This suggests that among optically red, compact sources, the incidence of broad lines is higher in sources with a stronger UV excess. In other words, the strength of their v-shaped SEDs.

The correlation between v-shaped SEDs, compact morphologies and broad emission lines has been noted in the past (Kocevski et al. 2025; Hviding et al. 2025) and suggests that a blue rest-UV color is a key criterion to identifying broad-line emitters among this population. If this UV emission originates from the host galaxy (e.g., Jones et al. 2025), this could indicate that the LRD phenomenon is preferentially associated with systems with young stellar populations and low dust attenuation that intrinsically have blue rest-UV continuum slopes (Topping et al. 2024). Alternatively, it could imply that some component of the UV excess found in LRDs originates from the central engine, possibly in the form of dust-scattered AGN emission (Assef et al. 2020; Kocevski et al. 2023). Under this scenario, the observed diversity in UV slopes across the LRD population could reflect varying proportions of emission from the host galaxy and a baseline level of scattered light from the central engine.

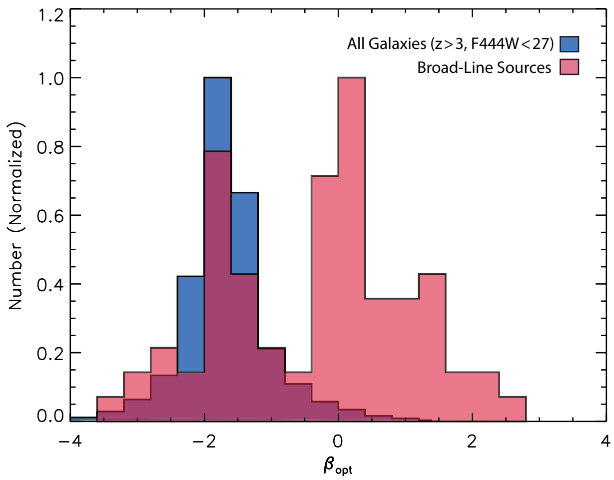

Figure 7. The rest-frame optical continuum slope, $\beta_{\rm opt}$, for bright (F444W $<$ 27) galaxies (blue histogram) and broad-line emitting sources (red histogram) in the CEERS field at $z > 3$. We find a bimodal distribution between LRDs and the bluest broad-line emitters with a minimum at $\beta_{\rm opt} \sim -1$.

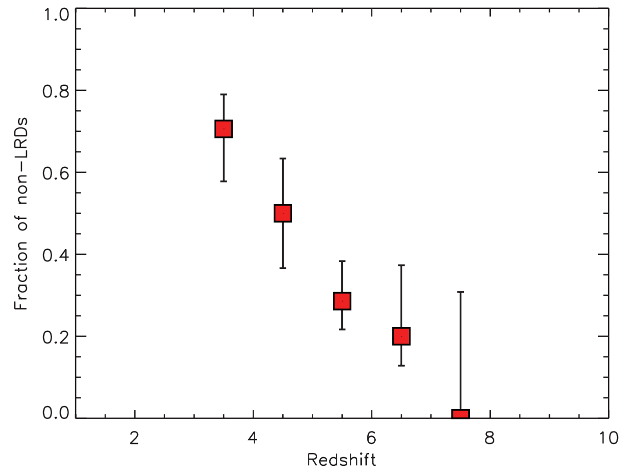

Figure 8. The observed fraction of blue broad-line emitting sources (i.e., non-LRDs) in the CEERS field as a function of redshift. Here blue is defined as $\beta_{\rm opt} < -0.52$. The fraction increases with decreasing redshift until the blue broad-line sources become the majority of the broad-line population at $z \sim 4$.

Lastly, we note that the broad-line detection fraction among both slope- and color-selected LRDs is strongly correlated with their F444W magnitude. This can be seen in the right-most panel of Figure 6. We find that the broad-line fraction among slope-selected LRDs with $\beta_{\rm opt} > -0.52$ drops from an average of $80.9^{+4.6}_{-7.5}\%$ for sources with F444W $<$ 26.5 to $53.3^{+11.7}_{-12.05}\%$ for sources with F444W $>$ 26.5. A commensurate decline is observed in color-selected LRDs. The Hα line luminosity of LRDs is closely correlated to their rest-optical continuum luminosity (Greene et al. 2024; de Graaff et al. 2025b), so we attribute this decline with F444W magnitude to the difficulty of finding and confirming broad emission components in sources with weaker emission lines.

8.1. *The Relationship Between LRDs and LBDs*

The connection between LRDs and their bluer counterparts, LBDs, remains a topic of debate. Recently defined by Brazzini et al. (2026) as compact sources with $\beta_{\rm opt} < 0$ and $\beta_{\rm UV} < -0.37$, LBDs share many of the same properties as LRDs, such as their X-ray weakness and a deficiency of hot dust emission, but generally lack Balmer absorption lines indicative of dense gas along the line of sight (Jones et al. 2025; Barro et al. 2026; Matthee et al. 2026; although see Scholtz et al. 2026; Davis et al. 2026). Our finding of a high broad-line detection fraction at bluer rest-optical colors ($\beta_{\rm opt} \sim -0.5$) indicates that the incidence of broad-line AGN extends beyond the reddest colors that define the canonical LRD selection and continues smoothly into the bluer regime occupied by LBDs. This would support the notion that LRDs are the extreme tail of a distribution of broad-line emitters that extends down to at least the reddest LBDs (Billand et al. 2026) and that these two populations differ primarily in their obscuration level (Madau & Maiolino 2026) or BH-to-galaxy luminosity ratio (Barro et al. 2026; Sun et al. 2026) rather than being two physically distinct classes of astrophysical objects.

That said, how LRDs and the reddest LBDs relate to the broad-line emitters found with the bluest rest-optical colors ($\beta_{\rm opt} \sim -2$) remains unclear (e.g., Hainline et al. 2025). When we examine the $\beta_{\rm opt}$ slope distribution of all broad-line emitters in the CEERS field (both LRDs and their blue counterparts), we find a bimodal distribution with relatively few broad-line sources at intermediate slopes ($\beta_{\rm opt} \sim -1$). This distribution can be seen in Figure 7, which shows the $\beta_{\rm opt}$ slopes for bright (F444W $<$ 27) galaxies and broad-line emitters detected in the CEERS field at $z > 3$.

Taken at face value, this bimodality would seem to argue against a simple unification model where all of the broad-line emitters are members of a single population that differ primarily by their level of obscuration as this would result in a more continuous $\beta_{\rm opt}$ distribution. However, the observed distribution is undoubtedly affected to some extent by selection effects since LRDs can be directly targeted, while blue broad-line emitters tend to be found serendipitously from among the general galaxy population. Further directed follow-up of sources with intermediate $\beta_{\rm opt}$ slopes will be needed to determine if the low incidence of broad-line emitters with "green" rest-optical colors is real. If this paucity is confirmed, it could indicate that the LRD phase, and its associated reddening, is rapid in its onset and completion and is distinct from the bluest broad-line emitters identified with JWST.

Recently Jones et al. (2025) noted that these blue broad-line sources are preferentially found at lower redshifts ($3 < z < 4$) and have lower BH-to-stellar mass ratios ($M_{\rm BH}/M_\star \sim 0.1\%$) compared to canonical LRDs. This is also borne out by our data and can be seen in Figure 8, which shows the observed fraction of blue broad-line emitters (here defined as $\beta_{\rm opt} < -0.52$, see §9) in the CEERS field as a function of redshift. We find the fraction steadily increases with decreasing redshift until the blue broad-line sources become the majority of the population around $z \sim 4$. It is important to note that the observed fraction does not represent the true abundance ratio between LRDs and non-LRDs as this would require correcting for the different selection effects that go into identifying them, a task that is beyond the scope of this paper. Nonetheless, the evolution of the observed fraction raises the possibility that the bluest broad-line emitters are more evolved versions of their redder counterparts, perhaps found after their dense gas cocoons have cleared and the stellar mass of their host galaxies has built up (e.g., Inayoshi 2025).

9. REVISED LRD SELECTION CRITERIA

In this section, we present a revised version of the LRD selection criteria of Kocevski et al. (2025) with changes that are informed by the continuum slope distribution of LRDs with confirmed broad-line detections. Given the persistently high broad-line fraction down to $\beta_{\rm opt} \sim -0.5$ and the bimodal $\beta_{\rm opt}$ distribution for broad-line emitters that reaches a minimum at $\beta_{\rm opt} \sim -1$, we propose the following criteria to identify compact objects with v-shaped SEDs and broad emission lines:

(i) $\beta_{\rm opt} > -0.52$

(ii) $-2.8 < \beta_{\rm UV} < -0.37$

(iii) $r_h < 1.5\ r_{h,\ \rm stars}$.

Here r_h is the half-light radius of the source measured in the F444W band and $r_{h,\ \rm stars}$ is the same value measured for stars.

We find that $80.9^{+4.6}_{-7.5}\%$ of bright sources (F444W $<$ 26.5) that satisfy these criteria in the CEERS field show broad emission lines. These new cuts effectively incorporate the reddest LBDs into the LRDs classification. Using this new definition, we find that LRDs make up 54% of all the faint, broad-line sources identified with JWST in the CEERS field.

The rest-optical slope cut of $\beta_{\rm opt} = -0.52$ corresponds to a F200W-F444W color of 0.75 at $z \sim 5$, which is slightly lower than the F200W $-$ F444W > 1 cut proposed by Barro et al. (2026). Using this lower threshold, we find the F115W-F200W versus F200W-F444W color wedge identifies 93% of the slope-selected LRDs, with the missing sources found at the extreme ends of the LRD redshift distribution, namely $z < 4$ and $z > 9$.

10. SUMMARY & CONCLUSIONS

In this paper, we present the Skyfire program, a 21-hour Cycle 3 JWST/NIRSpec survey with the G395M medium-resolution grating covering five pointings in the CEERS field. The survey is designed to perform a census of faint, broad-line AGN with a range of rest-optical colors at $z > 3$. The survey's primary targets include photometrically-selected LRDs, blue DLEs and X-ray detected AGN, while filler targets are chosen preferentially from among bright sources in F444W with photometric redshifts of $z > 3$.

Skyfire observed 292 sources and recovered secure redshifts for 178, including 34 LRDs, 20 DLE, and 3 X-ray sources. We find good agreement between our photometric and spectroscopic redshifts, with their difference having a scatter of $\sigma_{\rm NMAD} = 0.0348$. We find the LRDs have a scatter comparable to our filler sample, indicating that the unusual SEDs of LRDs do not result in an increased photometric redshift uncertainty similar to what is commonly found with other types of bright AGN.

In our spectroscopic sample, we identify a total of 34 sources with broad emission lines in the redshift range $2.7 < z < 6.5$. These lines have FWHMs ranging from 500 to 4000 km s^{-1}, the lowest of which likely originate from among the least massive SMBHs known in the early universe. Two LRDs in our sample have blue-shifted absorption in their Balmer emission lines. We also find that only 3/17 EELGs selected primarily based on their high-equivalent-width emission lines and compact morphologies exhibit broad emission lines, suggesting that these criteria alone are poorly predictive of broad-line activity.

With the completion of Skyfire, 73% of the photometrically-selected LRDs from the Kocevski et al. (2025) sample in the CEERS field have been observed spectroscopically. Combining Skyfire with spectroscopic redshifts and broad-line detections reported in the literature, we explore the prevalence of broad emission lines in LRDs as a function of their rest-frame continuum slope and observed color distributions. We find the broad-line detection fraction in LRDs remains high at bluer rest-optical colors, suggesting the incidence of broad-line AGN extends beyond the reddest colors that define the canonical LRD selection and extends smoothly into the bluer regime occupied by LBDs. This supports unification models that propose that LRDs and the reddest LBDs differ primarily in their obscuration level or BH-to-galaxy luminosity ratio rather than being two physically distinct classes of astrophysical objects.

We do, however, find a bimodal $\beta_{\rm opt}$ slope distribution between LRDs and broad-line sources with the bluest rest-optical colors. We show that the observed fraction of blue ($\beta_{\rm opt} < -0.52$) broad-line emitting sources increases with decreasing redshift until they become the majority of the broad-line population at $z \sim 4$. This raises the possibility that the bluest broad-line emitters may be more evolved versions of their redder counterparts, found after their dense gas cocoons have cleared out and the stellar mass of their host galaxies has built up.

We also find a low broad-line fraction in photometrically-selected LRD with the reddest rest-UV colors, suggesting the strength of the v-shape in the SEDs of LRDs is closely tied to the incidence of broad-line emission. This could imply that some component of the UV excess found in LRDs originates from the central engine and that the diversity in UV slopes across the LRD population is due to varying proportions of light from the host galaxy and a baseline level of emission from the central engine, possibly in the form of dust-scattered light.

Finally, we present revised LRD selection criteria for identifying compact objects with v-shaped SEDs and broad emission lines that extends down to $\beta_{\rm opt} = -0.52$. Using these criteria, we find that $80.9^{+4.6}_{-7.5}\%$ of bright (F444W < 26.5), photometrically-selected LRDs in the CEERS field have broad emission lines. With this lower $\beta_{\rm opt}$ threshold, we find that LRDs make up 54% of all the broad-line emitters found with JWST in the CEERS field.

In the future, we aim to use Skyfire to examine the spectra of individual sources of interest, as well as continue our study of LRD demographics, which is possible due to the high spectroscopic completeness achieved in the CEERS field. The data collected by Skyfire is publicly available and we welcome and encourage its use by the broader community.

11. ACKNOWLEDGMENTS

The Skyfire team would like to thank our program coordinators, Alaina Henry and Weston Eck, for their help with planning and executing our program. We also thank the previous surveys that contributed to making the EGS such a data rich field, including AEGIS, CANDELS, 3D-HST, CEERS, RUBIES, CAPERS, THRILS, C3PO, OCEANS, and MEGA. This work is supported by NASA grant JWST-GO-5718 based on observations made with the NASA/ESA/CSA James Webb Space Telescope. The data were obtained from the Mikulski Archive for Space Telescopes at the Space Telescope Science Institute, which is operated by the Association of Universities for Research in Astronomy, Inc., under NASA contract NAS 5-03127 for JWST.

APPENDIX

A. NIRSPEC SPECTRA OF BROAD LINE SOURCES

Here we present the G395M spectra of the 33 new Skyfire sources that show broad emission features, in regions near the broad component. These spectra, along with our best-fit two component (narrow plus broad) emission line model for each line, are shown in Figure 9.

REFERENCES

Arrabal Haro, P., Dickinson, M., Finkelstein, S. L., et al. 2023, Nature, 622, 707, doi: 10.1038/s41586-023-06521-7

Asada, Y., Inayoshi, K., Fei, Q., Fujimoto, S., & Willott, C. 2026, arXiv e-prints, arXiv:2601.10573, doi: 10.48550/arXiv.2601.10573

Assef, R. J., Brightman, M., Walton, D. J., et al. 2020, ApJ, 897, 112, doi: 10.3847/1538-4357/ab9814

Backhaus, B. E., Kirkpatrick, A., Yang, G., et al. 2025, AJ, 170, 300, doi: 10.3847/1538-3881/ae0cc4

Bagley, M. B., Finkelstein, S. L., Koekemoer, A. M., et al. 2022, arXiv e-prints, arXiv:2211.02495. https://arxiv.org/abs/2211.02495

Barro, G., Pérez-González, P. G., Kocevski, D. D., et al. 2024, ApJ, 963, 128, doi: 10.3847/1538-4357/ad167e

—. 2026, ApJ, 997, 48, doi: 10.3847/1538-4357/ae0704

Bertin, E., & Arnouts, S. 1996, A&AS, 117, 393, doi: 10.1051/aas:1996164

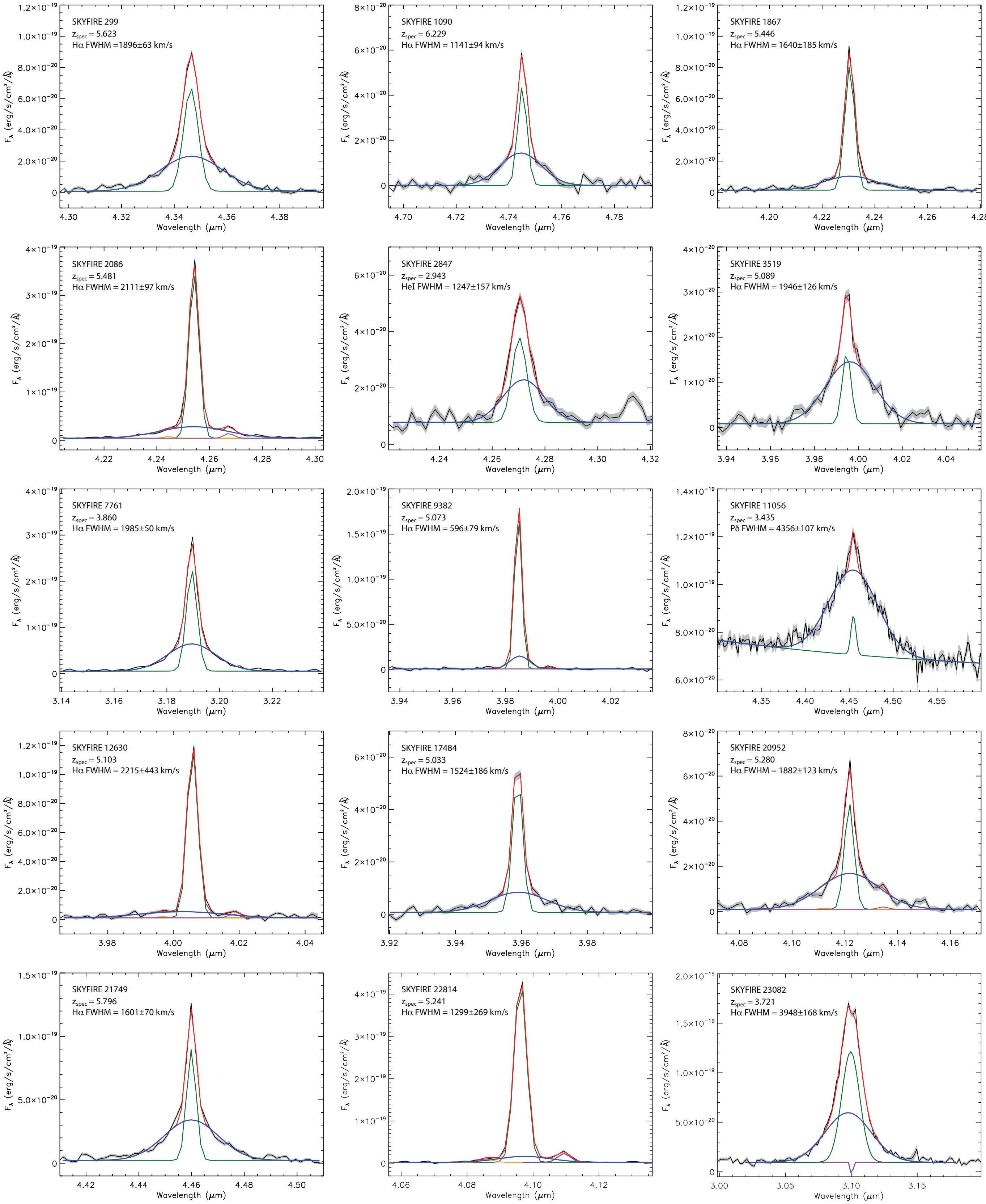

Figure 9. NIRSpec spectra with uncertainties (grey shaded region) taken in the G395M grating of Skyfire sources that feature broad emission lines detected at a SNR > 5. Green lines show the best-fit Gaussian for the narrow emission line component, blue lines show the best-fit broad component, and red lines show the best overall (narrow plus broad) fit the emission line. The FWHM of the broad component (corrected for instrument broadening) is shown in the upper left of each panel.

Billand, J.-B., Elbaz, D., Franco, M., et al. 2026, arXiv e-prints, arXiv:2604.11677, doi: 10.48550/arXiv.2604.11677

Bisigello, L., Euclid Collaboration, Rodighiero, G., et al. 2025, arXiv e-prints, arXiv:2503.15323, doi: 10.48550/arXiv.2503.15323

Bonaventura, N., Jakobsen, P., Ferruit, P., Arribas, S., & Giardino, G. 2023, A&A, 672, A40, doi: 10.1051/0004-6361/202245403

Brammer, G. B., van Dokkum, P. G., & Coppi, P. 2008, ApJ, 686, 1503, doi: 10.1086/591786

Brammer, G. B., van Dokkum, P. G., Franx, M., et al. 2012, ApJS, 200, 13, doi: 10.1088/0067-0049/200/2/13

Brazzini, M., D'Eugenio, F., Maiolino, R., et al. 2026, arXiv e-prints, arXiv:2601.22214, doi: 10.48550/arXiv.2601.22214

Casertano, S., de Mello, D., Dickinson, M., et al. 2000, AJ, 120, 2747, doi: 10.1086/316851

Chen, Z., Faber, S. M., Koo, D. C., et al. 2020, ApJ, 897, 102, doi: 10.3847/1538-4357/ab9633

Conroy, C., White, M., & Gunn, J. E. 2010, ApJ, 708, 58, doi: 10.1088/0004-637X/708/1/58

Dahlen, T., Mobasher, B., Faber, S. M., et al. 2013, ApJ, 775, 93, doi: 10.1088/0004-637X/775/2/93

Davé, R., Anglés-Alcázar, D., Narayanan, D., et al. 2019, MNRAS, 486, 2827, doi: 10.1093/mnras/stz937

Davis, K., Brooks, M., Simons, R. C., et al. 2026, arXiv e-prints, arXiv:2606.00258, doi: 10.48550/arXiv.2606.00258

Davis, M., Guhathakurta, P., Konidaris, N. P., et al. 2007, ApJL, 660, L1, doi: 10.1086/517931

de Graaff, A., Rix, H.-W., Carniani, S., et al. 2024, A&A, 684, A87, doi: 10.1051/0004-6361/202347755

de Graaff, A., Brammer, G., Weibel, A., et al. 2025a, A&A, 697, A189, doi: 10.1051/0004-6361/202452186

de Graaff, A., Hviding, R. E., Naidu, R. P., et al. 2025b, arXiv e-prints, arXiv:2511.21820, doi: 10.48550/arXiv.2511.21820

Di Matteo, T., Colberg, J., Springel, V., Hernquist, L., & Sijacki, D. 2008, ApJ, 676, 33, doi: 10.1086/524921

Donnan, C. T., Dickinson, M., Taylor, A. J., et al. 2025, ApJ, 993, 224, doi: 10.3847/1538-4357/ae0a1f

Dubois, Y., Peirani, S., Pichon, C., et al. 2016, MNRAS, 463, 3948, doi: 10.1093/mnras/stw2265

Fan, X., Narayanan, V. K., Lupton, R. H., et al. 2001, AJ, 122, 2833, doi: 10.1086/324111

Ferrarese, L., & Merritt, D. 2000, ApJL, 539, L9, doi: 10.1086/312838

Finkelstein, S. L., Bagley, M. B., Arrabal Haro, P., et al. 2022, arXiv e-prints, arXiv:2207.12474. https://arxiv.org/abs/2207.12474

Finkelstein, S. L., Leung, G. C. K., Bagley, M. B., et al. 2023, arXiv e-prints, arXiv:2311.04279, doi: 10.48550/arXiv.2311.04279

—. 2024, ApJL, 969, L2, doi: 10.3847/2041-8213/ad4495

Finkelstein, S. L., Bagley, M. B., Arrabal Haro, P., et al. 2025a, ApJL, 983, L4, doi: 10.3847/2041-8213/adbbd3

—. 2025b, ApJL, 983, L4, doi: 10.3847/2041-8213/adbbd3

Fruchter, A. S., & Hook, R. N. 2002, PASP, 114, 144, doi: 10.1086/338393

Furtak, L. J., Zitrin, A., Plat, A., et al. 2023, ApJ, 952, 142, doi: 10.3847/1538-4357/acdc9d

Gaia Collaboration, Prusti, T., de Bruijne, J. H. J., et al. 2016, A&A, 595, A1, doi: 10.1051/0004-6361/201629272

Galametz, A., Grazian, A., Fontana, A., et al. 2013, ApJS, 206, 10, doi: 10.1088/0067-0049/206/2/10

Gardner, J. P., Mather, J. C., Abbott, R., et al. 2023, PASP, 135, 068001, doi: 10.1088/1538-3873/acd1b5

Gebhardt, K., Bender, R., Bower, G., et al. 2000, ApJL, 539, L13, doi: 10.1086/312840

Greene, J. E., Labbe, I., Goulding, A. D., et al. 2024, ApJ, 964, 39, doi: 10.3847/1538-4357/ad1e5f

Grogin, N. A., Kocevski, D. D., Faber, S. M., et al. 2011, ApJS, 197, 35. https://arxiv.org/abs/1105.3753

Guo, J., Onoue, M., Inayoshi, K., et al. 2025, ApJ, 991, 74, doi: 10.3847/1538-4357/adee0f

Habouzit, M., Onoue, M., Bañados, E., et al. 2022, MNRAS, 511, 3751, doi: 10.1093/mnras/stac225

Hainline, K. N., Maiolino, R., Juodžbalis, I., et al. 2025, ApJ, 979, 138, doi: 10.3847/1538-4357/ad9920

Harikane, Y., Zhang, Y., Nakajima, K., et al. 2023, ApJ, 959, 39, doi: 10.3847/1538-4357/ad029e

Heintz, K. E., Watson, D., Brammer, G., et al. 2024, Science, 384, 890, doi: 10.1126/science.adj0343

Hopkins, P. F., Hernquist, L., Cox, T. J., & Kereš, D. 2008, ApJS, 175, 356, doi: 10.1086/524362

Horne, K. 1986, PASP, 98, 609, doi: 10.1086/131801

Hutchison, T. A., Larson, R. L., Arrabal Haro, P., et al. 2025, arXiv e-prints, arXiv:2512.12509, doi: 10.48550/arXiv.2512.12509

Hviding, R. E., de Graaff, A., Miller, T. B., et al. 2025, arXiv e-prints, arXiv:2506.05459, doi: 10.48550/arXiv.2506.05459

Ilbert, O., Capak, P., Salvato, M., et al. 2009, ApJ, 690, 1236, doi: 10.1088/0004-637X/690/2/1236

Inayoshi, K. 2025, ApJL, 988, L22, doi: 10.3847/2041-8213/adea66

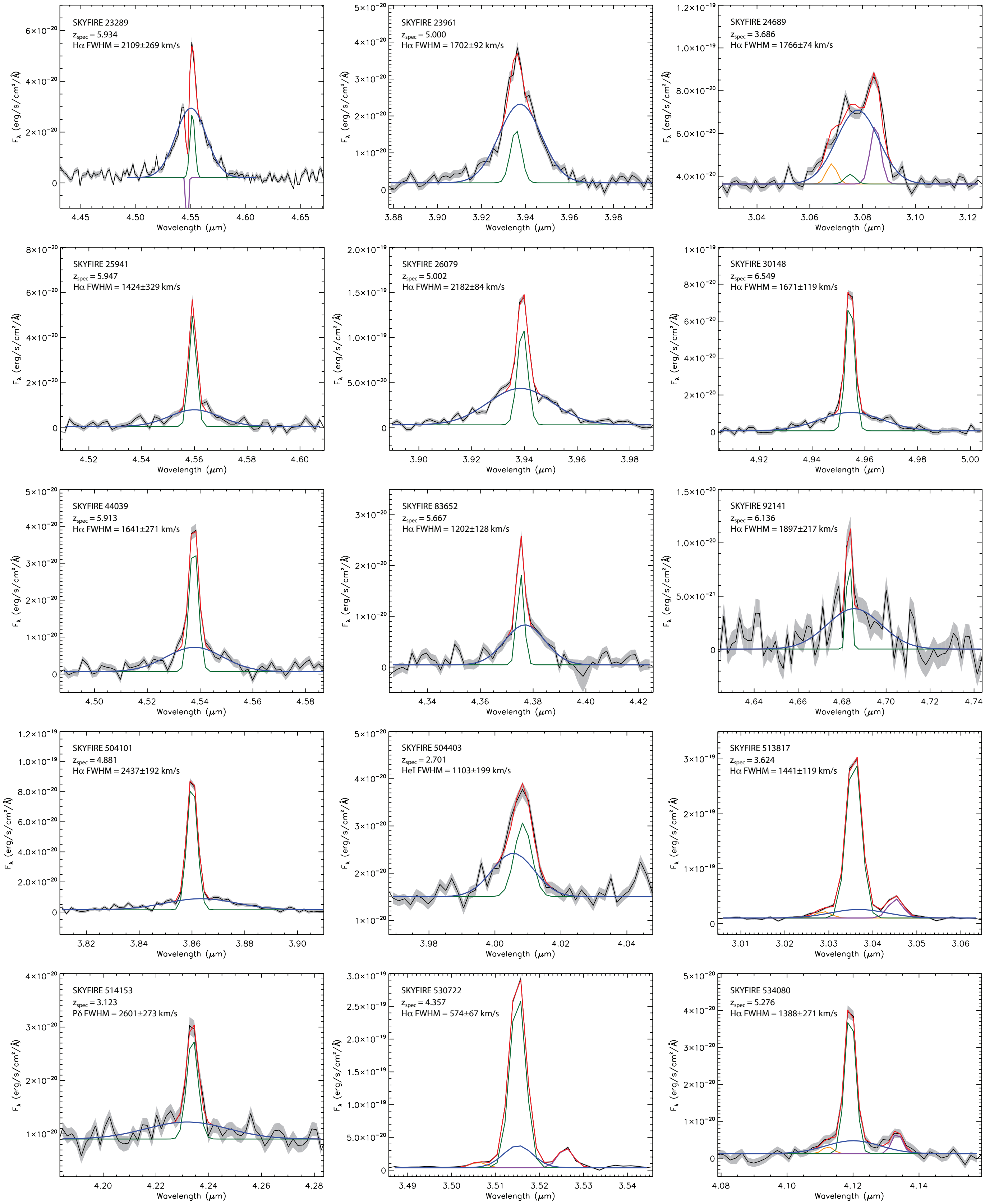

Figure 9 (Cont.). NIRSpec spectra with uncertainties (grey shaded region) taken in the G395M grating of Skyfire sources that feature broad emission lines detected at a SNR > 5. Green lines show the best-fit Gaussian for the narrow emission line component, blue lines show the best-fit broad component, and red lines show the best overall (narrow plus broad) fit the emission line. The FWHM of the broad component (corrected for instrument broadening) is shown in the upper left of each panel.

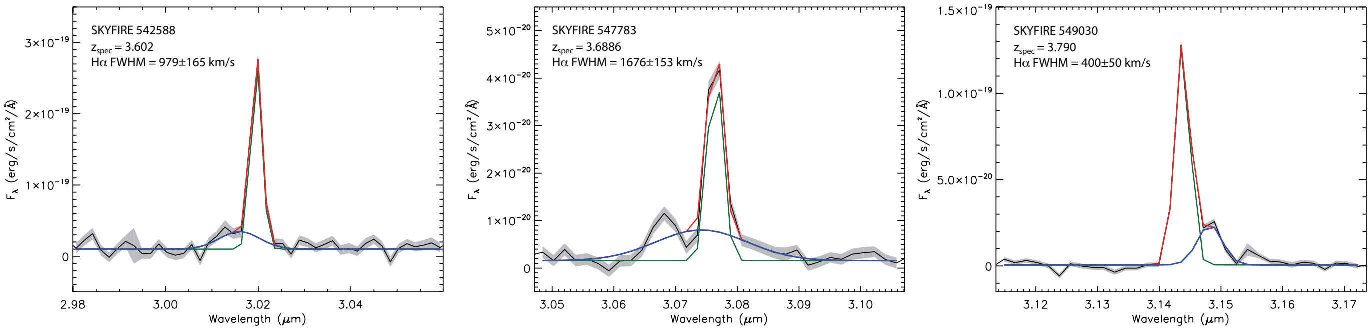

Figure 9 (Cont.). NIRSpec spectra with uncertainties (grey shaded region) taken in the G395M grating of Skyfire sources that feature broad emission lines detected at a SNR > 5. Green lines show the best-fit Gaussian for the narrow emission line component, blue lines show the best-fit broad component, and red lines show the best overall (narrow plus broad) fit the emission line. The FWHM of the broad component (corrected for instrument broadening) is shown in the upper left of each panel.

Inayoshi, K., & Maiolino, R. 2025, ApJL, 980, L27, doi: 10.3847/2041-8213/adaebd

Inayoshi, K., Nakatani, R., Toyouchi, D., et al. 2022, ApJ, 927, 237, doi: 10.3847/1538-4357/ac4751

Inayoshi, K., Visbal, E., & Haiman, Z. 2020, ARA&A, 58, 27, doi: 10.1146/annurev-astro-120419-014455

Jiang, L., McGreer, I. D., Fan, X., et al. 2016, ApJ, 833, 222, doi: 10.3847/1538-4357/833/2/222

Jones, B. L., Kocevski, D. D., Pacucci, F., et al. 2025, arXiv e-prints, arXiv:2510.07376, doi: 10.48550/arXiv.2510.07376

Jung, I., Finkelstein, S. L., Livermore, R. C., et al. 2018, ApJ, 864, 103, doi: 10.3847/1538-4357/aad686

Juodžbalis, I., Marconcini, C., D'Eugenio, F., et al. 2025, arXiv e-prints, arXiv:2508.21748, doi: 10.48550/arXiv.2508.21748

Kocevski, D. D., Onoue, M., Inayoshi, K., et al. 2023, ApJL, 954, L4, doi: 10.3847/2041-8213/ace5a0

Kocevski, D. D., Finkelstein, S. L., Barro, G., et al. 2025, ApJ, 986, 126, doi: 10.3847/1538-4357/adbc7d

Koekemoer, A. M., Faber, S. M., Ferguson, H. C., et al. 2011, ApJS, 197, 36. https://arxiv.org/abs/1105.3754

Kokorev, V., Caputi, K. I., Greene, J. E., et al. 2024, arXiv e-prints, arXiv:2401.09981, doi: 10.48550/arXiv.2401.09981

Kokorev, V., Chisholm, J., Naidu, R. P., et al. 2026, ApJ, 1004, 153, doi: 10.3847/1538-4357/ae4ed7

Kormendy, J., & Ho, L. C. 2013, ARA&A, 51, 511, doi: 10.1146/annurev-astro-082708-101811

Kormendy, J., & Richstone, D. 1995, ARA&A, 33, 581, doi: 10.1146/annurev.aa.33.090195.003053

Labbe, I., Greene, J. E., Bezanson, R., et al. 2023, arXiv e-prints, arXiv:2306.07320, doi: 10.48550/arXiv.2306.07320

—. 2025, ApJ, 978, 92, doi: 10.3847/1538-4357/ad3551

Larson, R. L., Finkelstein, S. L., Hutchison, T. A., et al. 2022, ApJ, 930, 104, doi: 10.3847/1538-4357/ac5dbd

Li, W., Inayoshi, K., Onoue, M., et al. 2024, ApJ, 969, 69, doi: 10.3847/1538-4357/ad46f9

Ma, Y., Greene, J. E., Setton, D. J., et al. 2025, arXiv e-prints, arXiv:2504.08032, doi: 10.48550/arXiv.2504.08032

Madau, P., & Dickinson, M. 2014, ARA&A, 52, 415, doi: 10.1146/annurev-astro-081811-125615

Madau, P., & Maiolino, R. 2026, arXiv e-prints, arXiv:2602.22386, doi: 10.48550/arXiv.2602.22386

Magorrian, J., Tremaine, S., Richstone, D., et al. 1998, AJ, 115, 2285, doi: 10.1086/300353

Maiolino, R., Scholtz, J., Curtis-Lake, E., et al. 2024, A&A, 691, A145, doi: 10.1051/0004-6361/202347640

Matsuoka, Y., Onoue, M., Kashikawa, N., et al. 2016, ApJ, 828, 26, doi: 10.3847/0004-637X/828/1/26

Matthee, J., Naidu, R. P., Brammer, G., et al. 2023, arXiv e-prints, arXiv:2306.05448, doi: 10.48550/arXiv.2306.05448

—. 2024, ApJ, 963, 129, doi: 10.3847/1538-4357/ad2345

Matthee, J., Torralba, A., Pezzulli, G., et al. 2026, arXiv e-prints, arXiv:2603.17667, doi: 10.48550/arXiv.2603.17667

Naidu, R. P., Matthee, J., Katz, H., et al. 2025, arXiv e-prints, arXiv:2503.16596, doi: 10.48550/arXiv.2503.16596

Nandra, K., Laird, E. S., Aird, J. A., et al. 2015, ApJS, 220, 10, doi: 10.1088/0067-0049/220/1/10

Newman, J. A., Cooper, M. C., Davis, M., et al. 2013, ApJS, 208, 5, doi: 10.1088/0067-0049/208/1/5

Onoue, M., Inayoshi, K., Ding, X., et al. 2023, ApJL, 942, L17, doi: 10.3847/2041-8213/aca9d3

Pacucci, F., Ferrara, A., & Kocevski, D. D. 2026, arXiv e-prints, arXiv:2601.14368, doi: 10.48550/arXiv.2601.14368

Pacucci, F., & Loeb, A. 2022, MNRAS, 509, 1885, doi: 10.1093/mnras/stab3071

Pacucci, F., Nguyen, B., Carniani, S., Maiolino, R., & Fan, X. 2023, ApJL, 957, L3, doi: 10.3847/2041-8213/ad0158

Pérez-González, P. G., Barro, G., Carniani, S., et al. 2026, arXiv e-prints, arXiv:2602.20247, doi: 10.48550/arXiv.2602.20247

Pirzkal, N., Malhotra, S., Ryan, R. E., et al. 2017, ApJ, 846, 84, doi: 10.3847/1538-4357/aa81cc

Reines, A. E., Greene, J. E., & Geha, M. 2013, ApJ, 775, 116, doi: 10.1088/0004-637X/775/2/116

Reines, A. E., & Volonteri, M. 2015, ApJ, 813, 82, doi: 10.1088/0004-637X/813/2/82

Rusakov, V., Watson, D., Nikopoulos, G. P., et al. 2025, arXiv e-prints, arXiv:2503.16595, doi: 10.48550/arXiv.2503.16595

Salvato, M., Hasinger, G., Ilbert, O., et al. 2009, ApJ, 690, 1250, doi: 10.1088/0004-637X/690/2/1250

Sanders, R. L., Shapley, A. E., Jones, T., et al. 2021, ApJ, 914, 19, doi: 10.3847/1538-4357/abf4c1

Scholtz, J., D'Eugenio, F., Maiolino, R., et al. 2026, arXiv e-prints, arXiv:2603.22277, doi: 10.48550/arXiv.2603.22277

Somerville, R. S., Hopkins, P. F., Cox, T. J., Robertson, B. E., & Hernquist, L. 2008, MNRAS, 391, 481, doi: 10.1111/j.1365-2966.2008.13805.x

Stefanon, M., Yan, H., Mobasher, B., et al. 2017, ApJS, 229, 32, doi: 10.3847/1538-4365/aa66cb

Sun, W. Q., Naidu, R. P., Matthee, J., et al. 2026, The Open Journal of Astrophysics, 9, 62505, doi: 10.33232/001c.162505

Taylor, A. J., Finkelstein, S. L., Kocevski, D. D., et al. 2025a, ApJ, 986, 165, doi: 10.3847/1538-4357/add15b

Taylor, A. J., Kokorev, V., Kocevski, D. D., et al. 2025b, ApJL, 989, L7, doi: 10.3847/2041-8213/ade789

Topping, M. W., Stark, D. P., Endsley, R., et al. 2024, MNRAS, 529, 4087, doi: 10.1093/mnras/stae800

Übler, H., Maiolino, R., Curtis-Lake, E., et al. 2023, arXiv e-prints, arXiv:2302.06647, doi: 10.48550/arXiv.2302.06647

Urbano Stawinski, S. M., Cooper, M. C., Finkelstein, S. L., et al. 2024, MNRAS, 528, 5624, doi: 10.1093/mnras/stae361

Volonteri, M. 2010, A&A Rv, 18, 279, doi: 10.1007/s00159-010-0029-x

Weibel, A., Naidu, R. P., Oesch, P. A., et al. 2026, arXiv e-prints, arXiv:2606.17271, doi: 10.48550/arXiv.2606.17271

Willott, C. J., Albert, L., Arzoumanian, D., et al. 2010, AJ, 140, 546, doi: 10.1088/0004-6256/140/2/546

Yang, G., Caputi, K. I., Papovich, C., et al. 2023a, ApJL, 950, L5, doi: 10.3847/2041-8213/acd639

Yang, J., Fan, X., Gupta, A., et al. 2023b, arXiv e-prints, arXiv:2302.01777, doi: 10.48550/arXiv.2302.01777

Zhuang, M.-Y., Li, J., Shen, Y., et al. 2025, arXiv e-prints, arXiv:2505.20393, doi: 10.48550/arXiv.2505.20393